

## Motion-map constrained image reconstruction (MCIR): Application to four-dimensional cone-beam computed tomography

Justin C. Park, Jin Sung Kim, Sung Ho Park, Zhaowei Liu, Bongyong Song, and William Y. Song

Citation: *Medical Physics* **40**, 121710 (2013); doi: 10.1118/1.4829504

View online: <http://dx.doi.org/10.1118/1.4829504>

View Table of Contents: <http://scitation.aip.org/content/aapm/journal/medphys/40/12?ver=pdfcov>

Published by the [American Association of Physicists in Medicine](#)

---



**DoseWise in the OR**  
10 easy steps for effective dose management

These steps help you adhere closely to the ALARA principle (As Low As Reasonably Achievable) for X-ray dose management.

- 1. Proper system setup**  
Correctly set up the system to ensure optimal image quality and dose management.
- 2. Use protective shielding**  
Use protective shielding to reduce patient and staff dose.
- 3. Remove X-ray grid**  
Remove the X-ray grid when not needed to reduce dose.
- 4. Position image detector**  
Position the image detector correctly to reduce dose.
- 5. Maintain distance**  
Maintain a safe distance from the X-ray source to reduce dose.

Teach your staff to be DoseWise.  
Order your free poster now!

 [www.philips.com/dosewiseintheor](http://www.philips.com/dosewiseintheor) **PHILIPS**

# Motion-map constrained image reconstruction (MCIR): Application to four-dimensional cone-beam computed tomography

Justin C. Park<sup>a)</sup>

*Center for Advanced Radiotherapy Technologies and Department of Radiation Medicine and Applied Sciences, University of California San Diego, La Jolla, California 92093 and Department of Electrical and Computer Engineering, University of California San Diego, La Jolla, California 92093*

Jin Sung Kim

*Department of Radiation Oncology, Samsung Medical Center, Seoul 135-710, South Korea*

Sung Ho Park

*Department of Medical Physics, Asan Medical Center, College of Medicine, University of Ulsan, Seoul 138-736, South Korea*

Zhaowei Liu

*Department of Electrical and Computer Engineering, University of California San Diego, La Jolla, California 92093*

Bongyong Song<sup>b)</sup> and William Y. Song

*Center for Advanced Radiotherapy Technologies and Department of Radiation Medicine and Applied Sciences, University of California San Diego, La Jolla, California 92093*

(Received 29 April 2013; revised 21 October 2013; accepted for publication 22 October 2013; published 12 November 2013)

**Purpose:** Utilization of respiratory correlated four-dimensional cone-beam computed tomography (4DCBCT) has enabled verification of internal target motion and volume immediately prior to treatment. However, with current standard CBCT scan, 4DCBCT poses challenge for reconstruction due to the fact that multiple phase binning leads to insufficient number of projection data to reconstruct and thus cause streaking artifacts. The purpose of this study is to develop a novel 4DCBCT reconstruction algorithm framework called motion-map constrained image reconstruction (MCIR), that allows reconstruction of high quality and high phase resolution 4DCBCT images with no more than the imaging dose as well as projections used in a standard free breathing 3DCBCT (FB-3DCBCT) scan.

**Methods:** The unknown 4DCBCT volume at each phase was mathematically modeled as a combination of FB-3DCBCT and phase-specific update vector which has an associated motion-map matrix. The motion-map matrix, which is the key innovation of the MCIR algorithm, was defined as the matrix that distinguishes voxels that are moving from stationary ones. This 4DCBCT model was then reconstructed with compressed sensing (CS) reconstruction framework such that the voxels with high motion would be aggressively updated by the phase-wise sorted projections and the voxels with less motion would be minimally updated to preserve the FB-3DCBCT. To evaluate the performance of our proposed MCIR algorithm, we evaluated both numerical phantoms and a lung cancer patient. The results were then compared with the (1) clinical FB-3DCBCT reconstructed using the FDK, (2) 4DCBCT reconstructed using the FDK, and (3) 4DCBCT reconstructed using the well-known prior image constrained compressed sensing (PICCS).

**Results:** Examination of the MCIR algorithm showed that high phase-resolved 4DCBCT with sets of up to 20 phases using a typical FB-3DCBCT scan could be reconstructed without compromising the image quality. Moreover, in comparison with other published algorithms, the image quality of the MCIR algorithm is shown to be excellent.

**Conclusions:** This work demonstrates the potential for providing high-quality 4DCBCT during on-line image-guided radiation therapy (IGRT), without increasing the imaging dose. The results showed that (at least) 20 phase images could be reconstructed using the same projections data, used to reconstruct a single FB-3DCBCT, without streak artifacts that are caused by insufficient projections.  
© 2013 American Association of Physicists in Medicine. [<http://dx.doi.org/10.1118/1.4829504>]

Key words: MCIR, 4DCBCT, iterative image reconstruction, compressed sensing, IGRT

## 1. INTRODUCTION

Currently, image guided radiation therapy (IGRT) utilizing external imaging devices to verify patient pose just before/during treatment is widely used.<sup>1,2</sup> In particular, cone-beam computed tomography (CBCT) is a commonly used imaging device mounted on linear accelerators for IGRT, due to its useful role in providing patients' (1) anatomic information,<sup>3,4</sup> (2) geometric information,<sup>5,6</sup> and (3) CT numbers for possible dose calculations and on-line/off-line reoptimization of plans.<sup>7,8</sup> With aid of CBCT, the implementation of various image guidance and adaptive techniques became possible.<sup>9-12</sup> There is minimal doubt that CBCT has a prominent role in current radiotherapy practices.

The CBCT acquisition time is long (typically 1 min for thoracic/abdominal sites) due to limited speed of the linear accelerator gantry.<sup>13-15</sup> In addition, there are challenges in verifying the trajectory of mobile tumors caused by breathing. For example, when CBCT is applied to thorax, the image quality can be heavily degraded due to the respiratory-induced motion. Serious motion-induced artifacts compromise the effectiveness of the CBCT usage during IGRT.<sup>16</sup>

To overcome this problem, four-dimensional CBCT (4DCBCT) has been proposed to provide time/phase-resolved volumetric images.<sup>17-21</sup> In such, all of the x-ray projections are first retrospectively grouped into different respiratory phase bins according to the breathing signals tagged to each projection. A 3DCBCT image set, for each breathing phase, is then reconstructed independently, yielding an image with much less motion-induced artifacts. The capability of 4DCBCT to significantly reduce the motion artifacts and enhance the target localization accuracy has been evaluated, allowing up to 50% reduction in planning target volume (PTV) size.<sup>22,23</sup>

Although 4DCBCT is capable of improving the motion artifacts and target localization accuracy, it poses another challenge for reconstruction. In fact, unless oversampling of x-ray projections are taken (which unavoidably increases the imaging dose<sup>17,22,23</sup>), the phase binning approach leads to insufficient number of projections in each phase bin and thus causes severe streaking artifacts, when a standard 3DCBCT scanning protocol and reconstruction algorithms [e.g., FDK (Ref. 24)] are applied. This is also known as the under-sampled artifact where the number of projections is insufficient to reconstruct a reasonable quality CBCT images.

In the past, many attempts have been made toward removing or relieving this problem. For example, scanning protocols of multiple gantry rotations and slow gantry rotations have both been proposed to considerably increase the number of projections per phase.<sup>19,21,25</sup> In either case, reducing the mAs to avoid increasing the imaging dose to patients inevitably degrades image quality. Advanced reconstruction techniques have also been proposed. For example, motion estimation and correction methods have been incorporated into the reconstruction process.<sup>26</sup> It has also been proposed to split the reconstruction region according to a volume of interest and treat the reconstructions separately.<sup>27</sup> Meanwhile, a number of research efforts have been made on postpro-

cessing of the 4DCBCT images. For instance, a prior image-based approach<sup>28</sup> has been developed by first reconstructing a blurred CBCT image with all projections and then using it to estimate and remove the streaking artifacts. Deforming all phase images onto a single representative one has also been tried.<sup>29,30</sup> The efficacy of these approaches, however, largely depends on the accuracy of the algorithms involved, such as the deformable image registration algorithms. One of the most advanced approaches to date is the prior image constrained compressed sensing (PICCS) algorithm which can reconstruct high quality 4DCBCT without increasing the imaging dose.<sup>31</sup> It first reconstructs a prior 3D image by using all projections and then reconstructs each phase image by regularizing both the total variation of the image itself and the total variation of the difference from the prior image.<sup>32-34</sup> Due to its high quality imaging performance and relative simplicity of the algorithm, PICCS has been utilized in many different applications.<sup>32-34,51,52</sup>

In this study, we propose a novel 4DCBCT reconstruction algorithm called motion-map constrained image reconstruction (MCIR) that utilizes a motion-map to achieve high-quality images from highly under-sampled projections. The MCIR algorithm allows (1) reconstruction of high quality 4DCBCT images with no more than the imaging dose used in a standard 3DCBCT scan, and (2) high phase-resolved images with up to 20 phases using a typical clinical 3DCBCT scan. Comparisons of our novel approach with the standard FDK and PICCS algorithms are presented in detail using numerical phantoms and a clinical lung cancer patient case.

## 2. METHODS AND MATERIALS

### 2.A. 4DCBCT basics

A common goal of the CBCT reconstructions is to solve the problem of finding the unknown attenuation coefficients from the projections data acquired at various gantry angles. In 4DCBCT, the goal is to reconstruct multiple 3DCBCT image sets from the phase-resolved projections. To ensure high quality images, it is traditionally necessary to acquire enough projections at each phase bin, which inevitably increases imaging dose, otherwise the under-sampled projections would lead to artifact-rich images. The main contribution of our proposed MCIR algorithm is to address this issue by generating high quality images under the constraint of under-sampled projections via intelligently differentiating the moving voxels from the stationary ones.

### 2.B. The MCIR algorithm

The key intuition of the MCIR algorithm lies in the observation that when a patient exhibits respiratory motion, not all parts of the patient's anatomy are in motion. For example, the tissues inside the lungs (e.g., diaphragm and tumor) move significantly whereas tissues outside the lungs are nearly stationary (e.g., bones, muscles). Suppose we can distinguish voxels between the ones that are moving and stationary via what we call a "motion-map," then a series of phase images can be

reconstructed by updating the FB-3DCBCT with only those voxels that are moving according to that corresponding phase while keeping the voxels constant for those that are stationary. The main advantage of such an approach is that since the number of *mobile* voxels to be reconstructed in each phase is less than the total voxels in a 3DCBCT image, the overall unknowns in each phase is now (much) smaller. Therefore, there is now higher measurements-to-unknowns ratio to reconstruct higher quality images due to this distinction.

In this paper, the matrices are denoted as a boldface-uppercase letters and the vectors are denoted as a boldface-lowercase letters. In the MCIR algorithm, we represent the unknown phase image volume as

$$\begin{aligned} \mathbf{x}_{\text{phase}} &= \mathbf{x}_{3\text{D}} + \mathbf{U}^{1/2} \mathbf{k}_{\text{phase}} \quad \text{where } \mathbf{x}_{\text{phase}} \in \mathbb{R}_+^M, \\ \mathbf{U} &\in \mathbb{R}_+^{M \times M} \text{ and } \mathbf{k}_{\text{phase}} \in \mathbb{R}^M, \end{aligned} \quad (1)$$

where  $\mathbf{x}_{\text{phase}}$  = unknown 4DCBCT phase image,  $\mathbf{x}_{3\text{D}}$  = *a priori* reconstructed FB-3DCBCT (reconstructed with the FDK (Ref. 24) or SART (Ref. 35)),  $\mathbf{U}$  = diagonal motion-map matrix,  $M$  = volume dimension, and  $\mathbf{k}_{\text{phase}}$  = phase-specific update vector. Equation (1) illustrates that our approach is to start from the FB-3DCBCT and then identify the phase specific motion information by referencing the motion-map matrix  $\mathbf{U}$ . The diagonal motion-map matrix  $\mathbf{U}$  is defined mathematically as follows:

$$\mathbf{U} = \text{diag}\{a_1, a_2, a_3, \dots, a_M\} \quad \text{where } a_i = [0, 1]. \quad (2)$$

---


$$\text{TV}(\mathbf{x}) = \sum_{i,j,k} \sqrt{[x(i+1, j, k) - x(i, j, k)]^2 + [x(i, j+1, k) - x(i, j, k)]^2 + [x(i, j, k+1) - x(i, j, k)]^2}, \quad (4)$$

where  $i$ ,  $j$ , and  $k$  correspond to left-right (LR), anterior-posterior (AP), and cranial-caudal (CC) coordinates, respectively. Here, the elements of the vector  $\mathbf{x}$  are indexed by the 3D coordinates for notational simplicity. In this form, the first term in Eq. (3) is the fidelity term, which enforces the fidelity of  $\mathbf{x}_{\text{phase}}$  with the sorted projection data. The second term, the regularization term, promotes sparsity inherent in the x-ray attenuation characteristics of the human body.

In Eq. (1), we have defined the 4DCBCT phase volume  $\mathbf{x}_{\text{phase}}$  as a combination of FB-3DCBCT with the phase-specific update vector  $\mathbf{k}_{\text{phase}}$  that is weighted by the motion-map matrix  $\mathbf{U}$ . The FB-3DCBCT,  $\mathbf{x}_{3\text{D}}$ , can be easily computed using all available projections. Assuming that we already know the motion-map matrix  $\mathbf{U}$ , which we will discuss in Sec. 2.C, we can solve Eq. (3). This is done by a gradient descent type approach where Eq. (1) is substituted into Eq. (3) and the gradient of the right-hand side of Eq. (3) with respect to  $\mathbf{k}_{\text{phase}}$  is calculated:

$$\begin{aligned} \mathbf{x}_{\text{phase}}^{n+1} &= \mathbf{x}_{\text{phase}}^n - \alpha \mathbf{U} [2\mathbf{A}_{\text{phase}}^T (\mathbf{A}_{\text{phase}} \mathbf{x}_{\text{phase}}^n - \mathbf{b}_{\text{phase}}) \\ &\quad + \lambda \nabla \text{TV}(\mathbf{x}_{\text{phase}}^n)], \end{aligned} \quad (5)$$

Here,  $a_i$  corresponds to the  $i$ th diagonal element of the matrix  $\mathbf{U}$ , where the value ranges between 0 and 1 with 1 when the voxel value varies largest with the respiratory motion and 0 when it is constant irrespective of breathing. The main reason for adding the square root term on  $\mathbf{U}$  in Eq. (1) is to simplify the updating equation for solving the  $\mathbf{x}_{\text{phase}}$ , which we will show shortly.

Remember that in 4DCBCT reconstruction, the projection data that are available for each phase is limited in number due to the binning process. Therefore, it is important to select reconstruction algorithm(s) that appropriately handles the situation to give you an adequate quality image. Recent studies have shown that compressed sensing type of CBCT reconstruction based on the total variation formulation has shown that efficient reconstruction can be performed with a limited number of projections.<sup>34,36-40</sup> Thus, utilizing this theory, keeping the phase volume  $\mathbf{x}_{\text{phase}}$  as an unknown, the mathematical model for the MCIR algorithm is setup to solve the constrained convex optimization of the form:

$$\begin{aligned} \min_{\mathbf{x}_{\text{phase}}} f(\mathbf{x}_{\text{phase}}) &= \|\mathbf{A}_{\text{phase}} \mathbf{x}_{\text{phase}} - \mathbf{b}_{\text{phase}}\|_2^2 + \lambda \text{TV}(\mathbf{x}_{\text{phase}}) \\ \text{s.t. } \mathbf{x}_{\text{phase}} &\geq 0, \end{aligned} \quad (3)$$

where  $\mathbf{A}_{\text{phase}}$  = Radon transform operator at a specific phase,  $\mathbf{b}_{\text{phase}}$  = phase sorted projection data,  $\lambda$  = regularization constant, and  $\text{TV}(\cdot)$  = total variation (TV) regularization term. The TV term we used in this study is defined as

---

where  $n$  = number of iterations,  $\alpha$  = gradient step size,  $\mathbf{A}_{\text{phase}}^T$  = back-projection matrix, and  $\nabla$  = gradient operator. Note here that by modeling the  $\mathbf{x}_{\text{phase}}$  with the square root  $\mathbf{U}$  [in Eq. (1)], the updating equation simplifies to multiplying with  $\mathbf{U}$ , instead of its square. A detailed derivation of Eq. (5) is presented in the Appendix.

In Eq. (5), we can notice that the gradient of the second term of Eq. (3) with respect to  $\mathbf{k}_{\text{phase}}$  simply becomes the product of  $\mathbf{U}$  with the  $\nabla \text{TV}$  (Ref. 40) (similar to taking the gradient with respect to  $\mathbf{x}_{\text{phase}}$ ). As a result, the updating energy will mainly be imparted on the voxels with the associated weighting factor  $a_i$  closer to 1 while spending little energy to update the voxels with values closer to 0. For those stationary voxels having  $a_i = 0$  in  $\mathbf{U}$ , will be preserved with the original values from the FB-3DCBCT,  $\mathbf{x}_{3\text{D}}$ .

## 2.C. Motion-map calculation

In Sec. 2.B, we have mathematically formulated the updating equation of the MCIR algorithm [Eq. (5)] to minimize the cost function given by Eq. (3). As you can imagine, calculating  $\mathbf{U}$  is a critical step in the implementation.

The effectiveness of the MCIR algorithm is largely dependent upon how well the motion-map represents the true mobile anatomy.

There can be a number of ways to calculate the motion-map of a patient. One intuitive way is to utilize a planning 4DCT dataset via calculation of deformable motion vectors. However, this approach may not be very useful since the patient posture must be very close, if not identical, between the 4DCT and at the time of the treatment. In addition, a considerable motion-to-motion variation on daily basis<sup>41</sup> as well as with registration uncertainty<sup>42</sup> exists which may hamper the precision of the motion-map.

In this study, we have developed a novel and effective method that obtains the motion-map directly from the phase-wise updated FB-3DCBCT. In this way, no external, prior-knowledge information is needed to obtain the motion map. The idea behind this concept is that when the FB-3DCBCT is reconstructed, the regions that are subject to varying degrees of respiratory motion would contain a larger data inconsistency (i.e., motion-induced artifacts) compared to the regions that are stationary. Intuitively, if we can incorporate such information and reconstruct with an effective strategy, a precise motion-map matrix  $U$  can be calculated. This is our intuition, which led to the following.

To calculate the motion-map matrix  $U$ , first, the FB-3DCBCT is reconstructed using all of the projections. For this, any reconstruction method can be used [e.g., the FDK (Ref. 24) or other compressed sensing type algorithms]. In this study, we used the FDK approach for its computational efficiency. Second, for each phase, the FB-3DCBCT is updated with the phase-wise sorted projection data while minimizing the one-norm difference from the original FB-3DCBCT as a regularization term. Third, the sub-motion-error vector for each phase, denoted by  $u_{\text{phase}}$ , is calculated by

taking the difference between the updated FB-3DCBCT with the original FB-3DCBCT. Mathematically, the sub-motion-error vector can be represented as

$$u_{\text{phase}} = x_{3D} - p_{\text{phase}}^* \quad \text{where } u_{\text{phase}} \in R^M \text{ and } p_{\text{phase}}^* \in R_+^M, \quad (6)$$

where

$$p_{\text{phase}}^* = \arg \min \left\{ \|A p_{\text{phase}} - b_{\text{phase}}\|_2^2 + \eta \|x_{3D} - p_{\text{phase}}\|_1 \right\} \quad \text{s.t. } p_{\text{phase}} \geq \mathbf{0}. \quad (7)$$

Here,  $p_{\text{phase}}$  = updated FB-3DCBCT with phase-wise sorted projection data with one-norm constraint,  $x_{3D}$  = *a priori* reconstructed FB-3DCBCT, and  $\eta$  = regularization constant for the one-norm term. In Eq. (7), we can notice that the original FB-3DCBCT,  $x_{3D}$ , is being updated with corresponding phase specific information,  $p_{\text{phase}}^*$ , while promoting sparsity in the difference between the original FB-3DCBCT and the updated value,  $p_{\text{phase}}$ . In this way, we can rigorously update the original FB-3DCBCT with phase information in the subvolumes that contain motion-induced data inconsistency while keeping the consistent regions with values from the original FB-3DCBCT. Then, by taking the difference between the FB-3DCBCT and  $p_{\text{phase}}^*$ , the sub-motion-error vector  $u_{\text{phase}}$  can be calculated, representing the motion-errors corresponding to each phase. Finally, when sub-motion-error vector has been calculated for all phases, we define the  $i$ th diagonal element  $a_i$  of the normalized motion-map matrix  $U$  as

$$a_i = \sum_{\text{phase}=1}^N |u_{\text{phase}}(i)| / \max_{1 \leq j \leq M} \left\{ \sum_{\text{phase}=1}^N |u_{\text{phase}}(j)| \right\}, \quad (8)$$

where  $N$  = total number of phase bins that are sorted. Figure 1 illustrates the process of calculating  $U$ . It can be seen

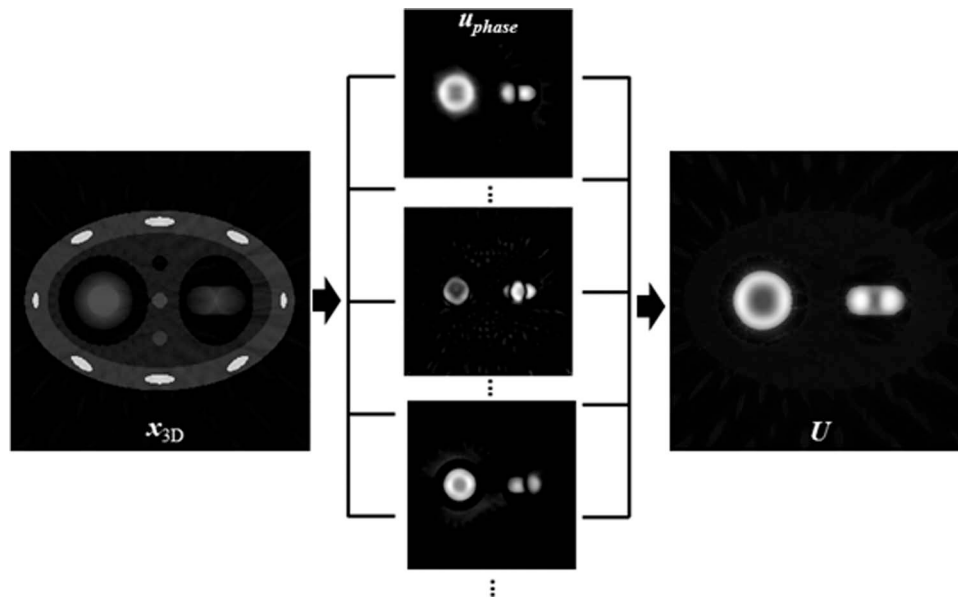


FIG. 1. Illustration of generating a motion-map,  $U$ . First,  $x_{\text{FB-3DCBCT}}$  is reconstructed using a conventional algorithm (e.g., FDK). Second, sub-motion-error vector for each phase ( $u_{\text{phase}}$ ) is calculated by taking the difference between the updated FB-3DCBCT with the original FB-3DCBCT. Finally, the motion-map matrix  $U$  is calculated by normalizing the absolute sum of sub-motion-error vector  $u_{\text{phase}}$  at all phases. As can be seen, image  $U$  exhibits very low values (dark  $\sim 0$ ), except near the circular objects that are moving (white  $\sim 1$ ).

TABLE I. Reconstruction times for each algorithm to process 100 iterations, for 20 phase images. All times are in seconds.

[Reconstruction Algorithms]	FDK	CS	PICCS	MCIR
Prior-image reconstruction	N/A	3.4	3.4	3.4
Motion map-calculation	N/A	N/A	N/A	64.5
Average comp. time/iteration	N/A	14.2	14.6	14.4
Total comp. time	4.1	1422.7	1467.1	1507.8

that a large proportion of  $\mathbf{U}$  exhibits very low values (close to 0) except the regions that contain significant motion.

Note that Eq. (7) to acquire the phase updated FB-3DCBCT is similar to Eq. (3), which is the main mathematical formulation of the MCIR algorithm. The main difference between the two is that when solving Eq. (3), the unknown 4DCBCT volume is mathematically modeled as a combination of FB-3DCBCT and phase-specific update vector associated with the motion map matrix  $\mathbf{U}$  [Eq. (1)], whereas in Eq. (7), such model cannot be applied since the motion map matrix  $\mathbf{U}$  is unknown. Moreover, the main purpose of solving Eq. (7) is to identify the regions that are inconsistent with the phase specific projection data and therefore, the one-norm difference term between the FB-3DCBCT and  $\mathbf{p}_{\text{phase}}$  is used as a regularization term to promote as many identical voxels between them as possible. On the other hand, Eq. (3) uses the TV regularization term to promote attenuation characteristics that improves the overall image quality.

Solving Eq. (7) for all phases can be a time-consuming task. Fortunately, it turns out that approximately solving the problem with only a few iterations provides enough information for generating the desired motion-map. As a result, the motion-map can be generated with much less computations compared to that required for reconstructing the 4DCBCT phase images, indicating that the overall overhead for generating the motion-map is relatively small. See Table I for a list of time commitments per task.

## 2.D. MCIR implementation

After the motion-map  $\mathbf{U}$  is generated, Eq. (5) has all of the necessary data to iteratively search for the best solution, for each 4DCBCT phase, with the original FB-3DCBCT as the

starting point. The MCIR algorithm pseudo code is laid out in Fig. 2. The process is as follows. First, the FB-3DCBCT is reconstructed with the FDK algorithm using all x-ray projections that were obtained. Second, the FB-3DCBCT is updated with phase-wise sorted projections such that regions containing the motion induced data inconsistency are updated with the phase information while enforcing consistency on the motion-free regions with the original values from the FB-3DCBCT. The updated volume is subtracted with the original FB-3DCBCT to generate the sub-motion-error vector,  $\mathbf{u}$ , for each phase. Third, the absolute values of the sub-motion-error vectors are element-wise added and normalized to the maximum value to obtain the motion-map matrix  $\mathbf{U}$ . Finally, for all phases, the MCIR is performed by initializing all voxels as the original FB-3DCBCT and updating the values according to Eq. (5), at each iterative step.

As can be noticed, the MCIR algorithm is an iterative process, which is computationally heavy, taking hours of CPU time ( $\sim 24\text{--}30$  h) to reach the solution. Efficiently solving this would require (1) parallel programming with proper hardware, and (2) deriving a mathematical formulation to achieve fast-solution-convergence. To handle the former issue, we have parallelized our code with the graphics processing unit (GPU) in the CUDA C/C++ programming environment. In this way, major computational tasks such as (1) forward projection, (2) back projection, and (3) vector as well as filter operations can be efficiently parallelized.<sup>43–45</sup> For the latter issue, we have used our recently published gradient projection algorithm based on the Barzilai-Borwein (GPBB) formulation that can handle compressed sensing type of CBCT reconstruction based on total variation formulation in an extremely efficient manner.<sup>40,46</sup> The main advantage of the GPBB approach is to use a minimal number of forward- and back-projections per iteration all at while ensuring fast convergence. By combining the GPBB approach with the massive parallelizable ability of the GPU programming, our recent work have shown that at least an order of magnitude faster reconstruction speed can be achieved.<sup>40,46</sup>

## 2.E. Numerical simulations and patient data

To evaluate the performance of our proposed MCIR algorithm, we have used both a numerical phantom and a clinical

Step 1: Input projection data $\mathbf{b}_{\text{All phase}}$
Step 2: Process FDK with $\mathbf{b}_{\text{All phase}}$ and set $\mathbf{x}_{3D} = \mathbf{x}_{\text{FDK}}$
Step 3: For each phase calculate sub-motion-error matrix $\mathbf{u}_{\text{phase}}$
Step 3-1: Set $\mathbf{p}_{\text{phase}}^0 = \mathbf{x}_{3D}$ and select $\mathbf{b}_{\text{phase}}$
Step 3-2: Iterate $\mathbf{p}_{\text{phase}}^{n+1} = \mathbf{p}_{\text{phase}}^n + \alpha [2\mathbf{A}_{\text{phase}}^T (\mathbf{A}_{\text{phase}} \mathbf{p}_{\text{phase}}^n - \mathbf{b}_{\text{phase}}) + \eta \text{sign}(\mathbf{x}_{3D} - \mathbf{p}_{\text{phase}}^n)]$
Step 3-3: Calculate $\mathbf{u}_{\text{phase}} = \mathbf{x}_{3D} - \mathbf{p}_{\text{phase}}^*$
Step 4: Set $\mathbf{U}$ according to Equations (6) & (7)
Step 5: For each phase process MCIR
Step 5-1: Set $\mathbf{x}_{\text{phase}}^0 = \mathbf{x}_{3D}$ and select $\mathbf{b}_{\text{phase}}$
Step 5-2: Iterate $\mathbf{x}_{\text{phase}}^{n+1} = \mathbf{x}_{\text{phase}}^n + \alpha \mathbf{U} [2\mathbf{A}_{\text{phase}}^T (\mathbf{A}_{\text{phase}} \mathbf{x}_{\text{phase}}^n - \mathbf{b}_{\text{phase}}) + \lambda \nabla \text{TV}(\mathbf{x}_{\text{phase}}^n)]$

FIG. 2. The MCIR algorithm pseudo code. Note here that the second term of the equation in step 3-2 is the first-order gradient of Eq. (7), and  $\text{sign}(\cdot)$  is the sign operation which is the first-order gradient of the 1-norm term in Eq. (7).

lung cancer patient with the x-ray projections obtained from the TrueBeam™ system (Varian Medical Systems, Palo Alto, CA). The results were then compared with the (1) clinical FB-3DCBCT reconstructed from the OBI™ using the FDK, (2) 4DCBCT reconstructed with the FDK, and (3) 4DCBCT reconstructed using the PICCS, a best-known 4DCBCT algorithm to date. For the numerical phantom study, we have used a dynamic chest phantom similar to those used in previous 4DCBCT related studies.<sup>28,47</sup> It is a numerical phantom that emulates respiratory motion with two circular objects that expand-shrink and move left-right (see Fig. 1). We first set the breathing period to 5 s with a cosine function and acquired 600 simulated projections over 1 min of a full gantry rotation, in a full-fan scanning geometry. We then divided and sorted the projections into even 20 phases. This means, on average, 30 projections were used to reconstruct each phase image.

For the clinical lung cancer patient case, a total of 674 projections were acquired over 1 min gantry rotation, in a half-fan scanning geometry, representing a typical FB-3DCBCT clinical scan. The imager has  $1024 \times 768$  pixels with  $0.388 \times 0.388$  mm<sup>2</sup> resolution. This was down-sampled to  $512 \times 384$  pixels with  $0.776 \times 0.776$  mm<sup>2</sup> for the reconstructions through two-by-two binning process. During the acquisition, each projection data was tagged with the phase information from the RPM™ system. Using this information, we divided and sorted the projections into 20 phases. On average, about 34 projections were assigned to each phase. The 4DCBCT volumes were reconstructed with  $512 \times 512 \times 70$  voxels at the resolution level of  $0.97 \times 0.97 \times 2.0$  mm<sup>3</sup>.

### 3. RESULTS

Figure 3 shows numerical 4D phantom simulation results including the ground truth images at two phases 0% and 50%, 4DCBCT reconstructed using the FDK, 4DCBCT reconstructed using the CS, 4DCBCT reconstructed using the PICCS, and 4DCBCT reconstructed using our MCIR algorithm. In order to ensure all iterative algorithms (CS, PICCS, and MCIR) to reach convergence as close as possible, we ran 1000 iterations for all with the same GP-BB step-size calculation approach.<sup>40,46</sup> Since the MCIR algorithm starts with a

FB-3DCBCT as an initial input, we have kept all initial input as FB-3DCBCT for the CS and PICCS algorithms as well. As is expected, a severe streaking artifacts appeared in the 4DCBCT reconstructed using the FDK algorithm [Figs. 3(b) and 3(g)]. Visually, many of the structures in the medial aspect of the phantom are nearly indistinguishable. 4DCBCT using the CS algorithm [Figs. 6(c) and 6(h)] significantly mitigated such artifacts, as expected. However, it was still evident that anatomical structures are blurred due to some patching artifacts (i.e., dark-gray streaks). As for the PICCS and MCIR, there are noticeable improvements in image quality from the CS [Figs. 6(d) and 6(i)]. Visually, the image quality seems nearly equivalent to each other. By taking a closer look, however, we see that the boundary of the moving balls in either side of the phantom is slightly sharper in the MCIR algorithm. Figure 4 shows the measured line profiles across the left ball in the phantom, for a 50% phase image. The line profile of the MCIR algorithm follows closest to the ground truth (see expanded view in the subset). In digging deeper, we have calculated the root mean square error (RMSE) for all 20 phase images, which is illustrated in Fig. 5. Here, the RMSE is defined as the root of the mean-squared percent error from the ground truth pixel values:

$$\text{RMSE}(\%) = \sqrt{\frac{\sum_{i,j,k} (x(i,j,k) - x(i,j,k)^{\text{Ground truth}})^2}{\sum_{i,j,k} (x(i,j,k)^{\text{Ground truth}})^2}} \times 100, \quad (9)$$

where,  $x(i,j,k)$  correspond to the voxel values in the reconstructed volume and  $x(i,j,k)^{\text{Ground truth}}$  refers to the ground truth voxel values of the numerical chest phantom that we used in this study. Looking at the error values for all phases, it is clear from the figure that the level of agreement to the ground truth is in the order of MCIR > PICCS > CS > FDK, for all phases. The FDK algorithm had the largest RMSE of  $30.0\% \pm 4.7\%$  ranging from 24.0% to 44.3%. The CS algorithm performed much better than FDK, which had RMSE of  $0.77\% \pm 0.13\%$  ranging from 0.4% to 1.14%. The RMSE for the PICCS varied from 0.43% to 0.75% with an average of  $0.52\% \pm 0.08\%$ . Finally, the MCIR algorithm showed the best performance

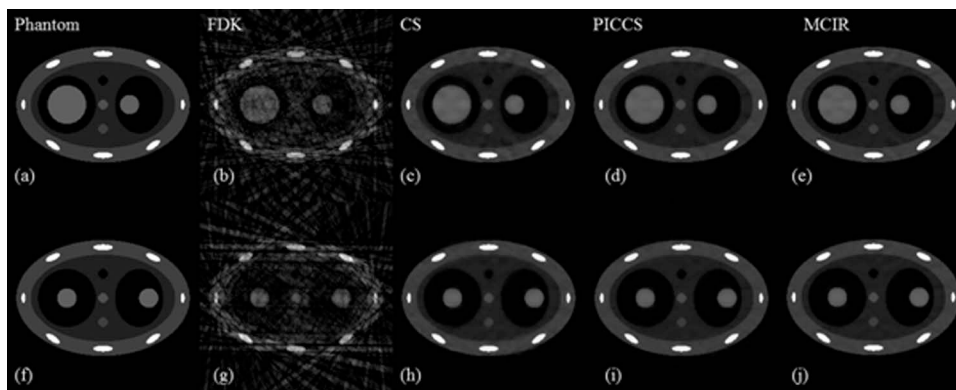


FIG. 3. A numerical 4D phantom simulation results. (a) and (f): ground truth phantom image at two phases 0% and 50%. (b) and (g): 4DCBCT reconstructed using the FDK. (c) and (h): 4DCBCT reconstructed using the CS. (d) and (i): 4DCBCT reconstructed using the PICCS. (e) and (j): 4DCBCT reconstructed using our MCIR algorithm.

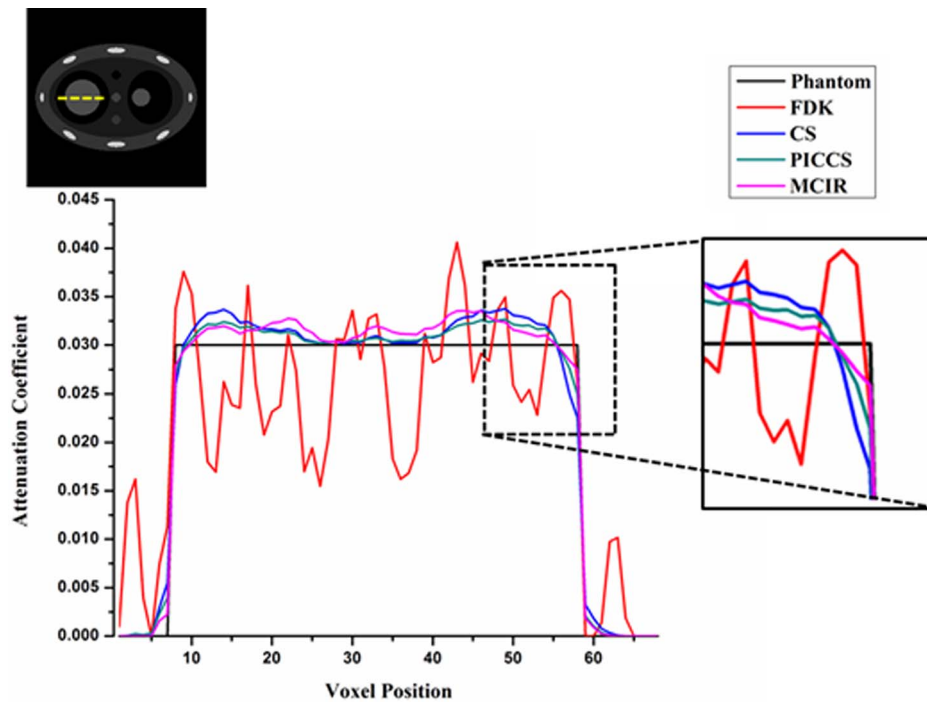


FIG. 4. Measured line profiles of the moving object in the 0% phase image.

with  $0.43\% \pm 0.04\%$  and ranged from 0.31% to 0.50%. This finding holds true at all levels of iterations as well, as shown in Fig. 6, where RMSE was calculated at each iterative step. As can be seen from the figure, the MCIR algorithm needs  $<100$  iterations to achieve RMSE  $<1\%$  from the ground truth, whereas the CS or PICCS need many more iterations to reach that level. This is mainly due to the fact that, unlike other algorithms, the update energy is mainly focused on the *mobile* voxels in our MCIR algorithm. This suggests that the MCIR algorithm outperforms the CS and PICCS, in terms of the final image quality (Fig. 5) and the speed of reaching the optimum solution is also faster (Fig. 6).

In order to demonstrate the relative computational speed for each algorithm, we have measured the time profile of the

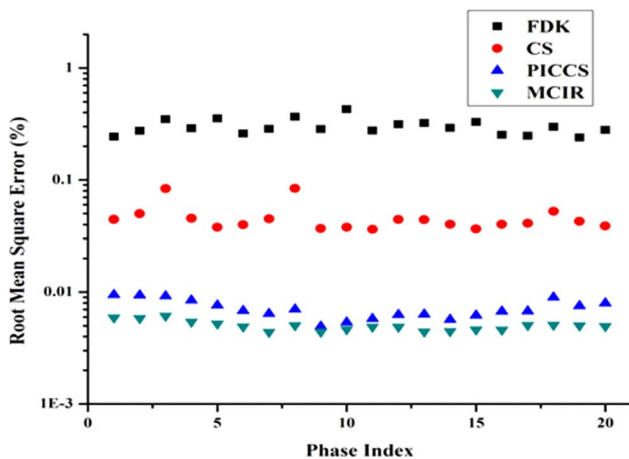


FIG. 5. Comparison of root mean square error (RMSE) between 4DCBCT reconstructed using the FDK, CS, PICCS, and our MCIR across all 20 phase images.

four different algorithms implemented on a single computer, with the same GPU and GPBB programming approaches, and kept all conditions the same. That is, the number of iterations was set to 100, the reconstruction volume was set to  $512 \times 512 \times 70$ , and 20 phases. Table I lists the times achieved. It was found that the MCIR algorithm takes slightly longer than the others since there is an additional step for computing the motion-map. The percentage of the total time increase, compared to the CS and PICCS, was 6% and 2%, respectively. However, since the convergence speed of the MCIR algorithm is significantly faster than the others (Fig. 6), such

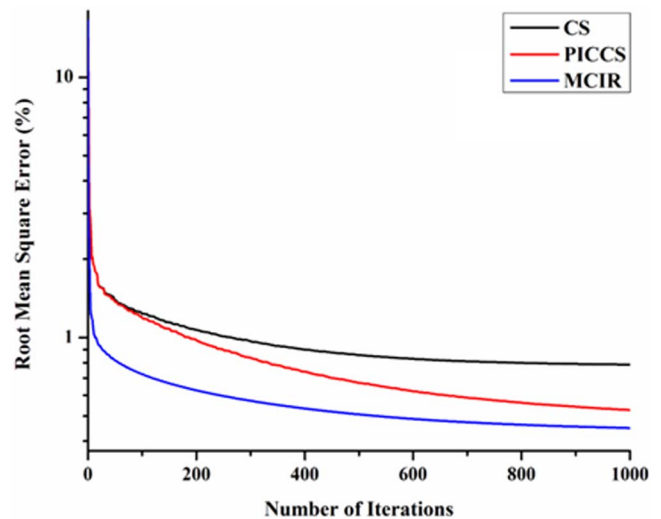


FIG. 6. Variation of RMSE calculated over each iterative step during the 4DCBCT reconstruction of 0% phase numerical phantom for the CS, PICCS, and the MCIR algorithm. Note that FDK is omitted from the comparison since it is not an iterative reconstruction algorithm.

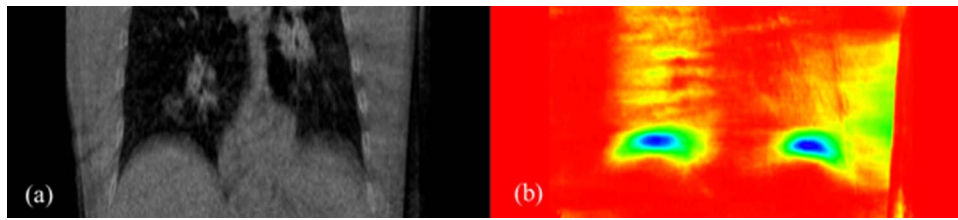


FIG. 7. (a) A coronal slice of FB-3DCBCT reconstructed using the clinical lung cancer patient data and (b) its corresponding motion-map using the proposed motion-map reconstruction approach. The motion-map intensity is the highest across the diaphragms as intuitively expected.

a difference can be compensated by reducing the total number of iterations while still achieving better image quality. For example, 100 iterations with the MCIR algorithm would achieve an RMSE  $< 1\%$ , whereas the CS or PICCS would need many more iterations to reach the same level.

Figure 7 shows a coronal slice of the FB-3DCBCT reconstructed using a clinical lung cancer patient data and its corresponding motion-map generated using the proposed motion-map reconstruction approach (in color scale from 0-1). As we expect from our clinical experience regarding thoracic anatomy, the motion-map intensity should be and is the highest around the diaphragms. It is also evident that the motion-map inside the lungs has varying degrees of intensity as well, which is also expected. One undesirable result, though, is that there is also some intensity in the soft tissue on the left side of the patient. This is due to the fact that the field of view (FOV) in our CBCT scanner is not enough to cover all of the patient's anatomy and, therefore, a truncation error would accumulate when the motion-map is generated. However, this is not an issue of concern as long as the motion-map captures all of the relevant part of the anatomy that are moving, which we absolutely need to visualize for 4D IGRT applications. In addition, since the motion-map is a weighting matrix that updates the initial FB-3DCBCT with phase-wise sorted projections that have already been used to reconstruct the original FB-3DCBCT, updating the nonmobile regions with the phase-wise sorted projections would be minimal, so there will not be much change in that region anyway.

Figure 8 shows coronal and sagittal slices of the lung cancer patient with the FB-3DCBCT, and the MCIR algorithm at 0%-peak-exhale, 25%-mid-inhale, 50%-peak-inhale,

and 75%-mid-exhale. It is clear that the image quality of the MCIR algorithm, at all phases, are almost equivalent to that of the FB-3DCBCT, in terms of low contrast and noise, but moreover, the diaphragm positions are clearly distinctive. This confirms that although only 34 projections were used to reconstruct each phase image, our MCIR algorithm can reconstruct all 20 phases of the breathing cycle without the agitating streak artifacts that are caused by insufficient projections.

Finally, Fig. 9 displays the lung cancer patient's 50% phase 4DCBCT image reconstructed with the FB-3DCBCT (using the FDK), 4D-FDK, MCIR, and the PICCS algorithms. As expected, severe streaking artifacts exist in the 4D-FDK. In contrast, both the MCIR and PICCS algorithms significantly outperform that of the 4D-FDK. In closer visual inspection, it is also observed that the streaking artifact is relatively further reduced in the MCIR algorithm as compared to the PICCS. For example, the diaphragm boundary shows reduced streaks.

## 4. DISCUSSION

### 4.A. Algorithm performance

In the evolution of lung cancer IGRT, transitioning from the FB-3DCBCT to 4DCBCT is essential due to the fact that the extent of tumor motion is the key information in maximizing the target localization accuracy.<sup>17, 18, 48-50</sup> With the use of conventional FDK reconstruction algorithm, the only way to achieve this is to increase the scanning time to acquire more projections, which inevitably increases the radiation exposure to patients. In this study, we proposed a novel 4DCBCT reconstruction approach called the MCIR, and have

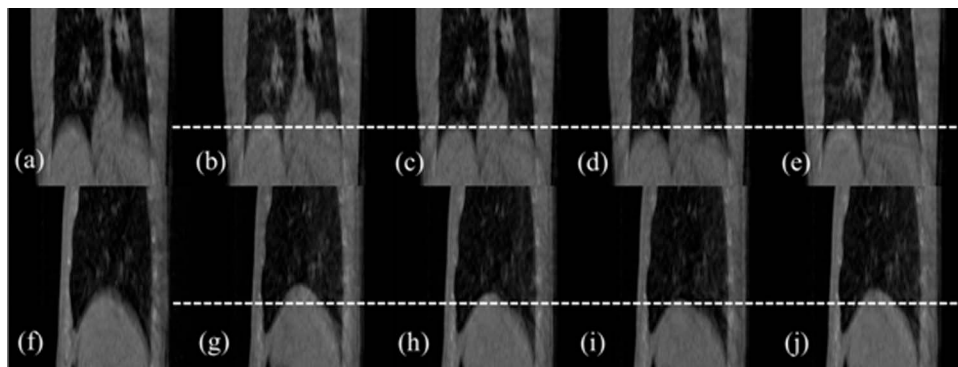


FIG. 8. Coronal and sagittal slices of the lung cancer patient of (a) and (f) FB-3DCBCT; and our proposed MCIR algorithm at (b) and (g) 0% phase; (c) and (h) 25% phase; (d) and (i) 50% phase; and (e) and (j) 75% phase. The image qualities of MCIR at all phases are almost equivalent to that of the FB-3DCBCT, but with the motion artifacts removed.

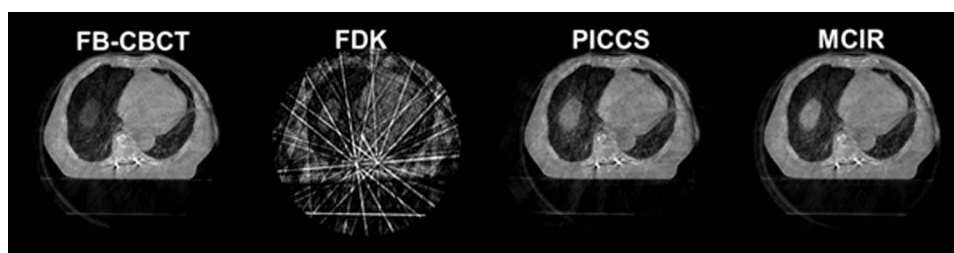


FIG. 9. An axial cut of the lung cancer patient reconstructed with the FB-3DCBCT, 4D-FDK, PICCS, and the MCIR algorithm.

successfully shown that at least up to 20 high quality phase images can be reconstructed using the same input dataset as a single clinical CBCT scan, without increasing the imaging dose. The main innovation comes from recognizing that when a thoracic anatomy is subjected to respiratory motion, not all parts of the anatomy are significantly moving. Therefore, if we could somehow distinguish between the regions that are moving more and less, we could reconstruct a high quality 4DCBCT by updating only the voxels with significant motion using the corresponding phase sorted projections while keeping the voxels that do not move from the FB-3DCBCT.

The results, both in numerical simulations as well as a patient data, showed that the MCIR algorithm outperforms many other popular-and-advanced algorithms such as the CS and PICCS. It should be noted though that the implementation of the CS and PICCS may not have been exactly reproduced as the ones originally proposed and implemented, as all of these algorithms were interpreted and written in-house. We attempted to make the fairest comparisons by implementing the codes as close to the publications as possible; however, it cannot be guaranteed that the same exact performance was observed. As a result, we fully acknowledge that our evaluation of these algorithms may not represent their best possible performance, although similarities such as the well-known patching artifact in the CS (Refs. 34, 51, and 52) was also readily observed in our implementation.

In addition to compressed-sensing based 4DCBCT reconstruction algorithms that we compared in this work, there are other 4DCBCT reconstruction frameworks that attempts to update motion-affected voxels. For example, the McKinnon-Bates (MKB) algorithm<sup>56,57</sup> uses a FB-3DCBCT as *a priori* image and uniformly updates the image with phase sorted projections with equal weight. Auto-adaptive phase correlation algorithm<sup>57</sup> weights the voxels that are moving and stationary and interpolates the motion voxels with the motion estimated projections within the filtered back-projection space. In contrast, the MCIR algorithm applies heavier weights to moving voxels while keeping lighter weights to stationary ones.

The performance of our MCIR algorithm is heavily dependent upon the quality of the FB-3DCBCT and the projection data. It was observed that when the initial quality of the FB-3DCBCT is poor, that propagated through the subsequent processing with the MCIR. This is, of course, quite obvious since the MCIR algorithm updates phase-specific information from the FB-3DCBCT as its base. Therefore, to maximize the performance of the MCIR algorithm, it is important to acquire high quality projection data, which will translate to

high quality FB-3DCBCT. There are numerous factors that could affect the quality of projection data such as CBCT scan geometry, x-ray exposure condition, and x-ray detector performance, etc. Low mAs settings can be one of the reasons of degradation in the quality due to the increase of quantum noise, for example. Use of preprocessing techniques such as scatter correction<sup>58,59</sup> and noise reduction<sup>60</sup> approaches on the projection data may be necessary to compensate for such degradations. Of course, this characteristic is also applicable to the PICCS algorithm since it uses the FB-3DCBCT as a prior knowledge.

The MCIR algorithm involves two independent iterative steps: (1) sub-motion-error vector, and (2) 4DCBCT calculations. In the clinical patient case, it was shown that  $\leq 6$  iterations were generally sufficient to calculate the sub-motion-error vector, and  $\leq 80$  iterations to generate the 4DCBCT. As a result, the overall overhead for computing the motion-map matrix is quite manageable.

#### 4.B. Motion-map estimation

Precise motion-map estimation is also an important factor that influences the performance of the MCIR algorithm. In this study, we proposed an effective method to obtain the motion-map directly from the x-ray projection data. Results showed that in both the numerical simulations and patient case, it effectively distinguished the regions that are stationary and moving. One limitation observed during the clinical patient case trial was that the accuracy of the motion-map can be degraded due to limited physical FOV size, leading to projection truncation error that would accumulate during the motion-map calculation.

However, as discussed, this is not a critical issue as long as the motion-map captures the real mobile regions of the thoracic anatomy, which is mostly within the lungs. Since motion-map is a weighting matrix designed to update the FB-3DCBCT using phase-wise sorted projections that have already been reconstructed into the initial FB-3DCBCT, updating the nonmoving regions with phase-wise sorted projections would have minimal effect in that region. Remember, the update equation of the MCIR is based on Eq. (1) where *a priori* calculated FB-3DCBCT image voxels are updated or kept constant depending on the subregions that are moving or stationary. The decision to update is defined by the magnitude of the motion map matrix  $U$ . If all of the voxels within the reconstructing region are moving, then all of the indices of  $U$  will be at or close to 1, which will then simply degenerate to the

conventional CS algorithm. Therefore, worst comes to worst, if the truncation artifacts are severe enough to affect the motion map of the entire reconstructing volume, it is expected that the resultant image would basically be equivalent to the quality of the conventional CS algorithm.

#### 4.C. Regularization parameters

In the MCIR algorithm, there are two different weighting parameters that need to be assigned: (1) the TV regularization parameter  $\lambda$  in Eq. (3) and (2) the one-norm regularization parameter  $\eta$  in Eq. (7). The former is one of the most influential parameters affecting the image quality, that is, when  $\lambda$  is high, the blurrier and smoother the images, and the smaller it is, the sharper and noisier the images. This is due to the fact that  $\lambda$  is a weighing factor of the TV regularization term in Eq. (3). Thus, if  $\lambda$  is high, more emphasis is given to minimize the total variance and therefore the blurrier but smoother the look. In opposite, if  $\lambda$  is low, then more emphasis will be given to the fidelity term in Eq. (3) and therefore preserving the noise and high frequency information.

The latter parameter  $\eta$  is the parameter that determines the sparseness of the motion map. The higher this value, more sparse the motion-map matrix (i.e., more zeros), which will emphasize the regions that has rigorous motion, while smaller this value, the motion-map matrix has less sparseness, giving nonzero values to regions that show relatively little movement. Therefore, when the *sparse* motion-map matrix,  $\mathbf{U}$ , is uploaded in the MCIR implementation, the result would be an image that rigorously emphasize only the voxels that has large data inconsistency due to breathing while other regions are left alone. Of course, it would be vice versa for the *less sparse* motion-map matrices.

Although some investigators have proposed ways to optimize the weighting parameters directly in the iterative optimization process,<sup>53,54</sup> there is no global standard in deterministically calculating them. Therefore, the selection of  $\lambda$  and  $\eta$  were subjectively picked through numerous repeat simulations.<sup>55</sup> In this study, we have set  $\lambda = 0.001$  and  $\eta = 0.5$  for the lung cancer patient case. It is obvious that further research is needed to find a class of optimal  $\lambda$  and  $\eta$  values for various clinical sites and patient sizes.

#### 4.D. Future work

In this study, we limited our investigation to one numerical phantom and a patient case. We learned that the proposed algorithm performs relatively well compared with other published algorithms and that reasonable quality 4DCBCT can be reconstructed using  $\sim 34$  projections per phase, at least, without major streak artifacts. Therefore, the next step is to test this algorithm on various clinical sites not only on lung but other moving anatomical sites such as liver or pancreas. Besides optimizing the performance of the MCIR algorithm, in terms of parameter selections, our next study will be to determine the optimal CBCT scanning protocols for use with the algorithm. We will comprehensively analyze what minimal number of projections, mAs, and scanning geometry can

work with the MCIR algorithm and still produce reasonable quality images for clinical use. Having said of all these limitations and the need for further investigations, our proposed MCIR algorithm is a promising new technique to generate a high quality 4DCBCT without increasing the imaging dose or scanning time, possibly enabling the frequent use of 4DCBCT for IGRT in the (hopefully) near future.

## 5. CONCLUSION

In this paper, we propose a novel 4DCBCT reconstruction algorithm utilizing a motion-map constraint as part of the framework. Up to 20 phases of clinically viable 4DCBCT images could be reconstructed while requiring no more projection data and imaging dose than a typical clinical 3DCBCT scan. This makes our MCIR algorithm potentially useful in an on-line IGRT environment.

## ACKNOWLEDGMENTS

This project is equally supported by National Research Foundation of Korea (NRF) Grant No. NRF-2011-0022021 funded by Ministry of Education, Science and Technology (MEST) and Radiation Safety Research Program No. 2011-31115 funded by Nuclear Safety and Security Commission. The authors report no conflicts of interest in conducting the research.

## APPENDIX: DERIVATION OF EQUATION 5

The cost function for MCIR algorithm is given by

$$\begin{aligned} \min_{\mathbf{x}_{\text{phase}}} f(\mathbf{x}_{\text{phase}}) &= \|\mathbf{A}_{\text{phase}}\mathbf{x}_{\text{phase}} - \mathbf{b}_{\text{phase}}\|_2^2 + \lambda TV(\mathbf{x}_{\text{phase}}) \\ \text{s.t. } \mathbf{x}_{\text{phase}} &\geq \mathbf{0}, \end{aligned} \quad (\text{A1})$$

where the unknown 4DCBCT volume at each phase can be expressed as

$$\mathbf{x}_{\text{phase}} = \mathbf{x}_{3D} + \mathbf{U}^{1/2}\mathbf{k}_{\text{phase}}. \quad (\text{A2})$$

Assuming that FB-3DCBCT volume  $\mathbf{x}_{3D}$  and the diagonal motion-map matrix is *a priori* computed, the gradient of convex function (A1) with respect to unknown vector  $\mathbf{k}_{\text{phase}}$  becomes

$$\begin{aligned} \nabla f(\mathbf{x}_{3D} + \mathbf{U}^{1/2}\mathbf{k}_{\text{phase}}) &= 2 \cdot (\mathbf{U}^{1/2})^T \mathbf{A}^T [\mathbf{A}(\mathbf{x}_{3D} + \mathbf{U}^{1/2}\mathbf{k}_{\text{phase}}) - \mathbf{b}_{\text{phase}}] \\ &\quad + \lambda \cdot \mathbf{U}^{1/2} \nabla TV(\mathbf{x}_{3D} + \mathbf{U}^{1/2}\mathbf{k}_{\text{phase}}). \end{aligned} \quad (\text{A3})$$

The updating equation for  $\mathbf{k}_{\text{phase}}$  at each iteration then becomes

$$\begin{aligned} \mathbf{k}_{\text{phase}}^{n+1} &= \mathbf{k}_{\text{phase}}^n - \alpha \nabla f(\mathbf{x}_{3D} + \mathbf{U}^{1/2}\mathbf{k}_{\text{phase}}^n) \\ &= \mathbf{k}_{\text{phase}}^n - \alpha (2 \cdot \mathbf{U}^{1/2} \mathbf{A}^T [\mathbf{A}(\mathbf{x}_{3D} + \mathbf{U}^{1/2}\mathbf{k}_{\text{phase}}^n) \\ &\quad - \mathbf{b}_{\text{phase}}] + \lambda \cdot \mathbf{U}^{1/2} \nabla TV(\mathbf{x}_{3D} + \mathbf{U}^{1/2}\mathbf{k}_{\text{phase}}^n)). \end{aligned} \quad (\text{A4})$$

Substituting Eq. (A4) into Eq. (1), we obtain

$$\begin{aligned} \mathbf{x}_{\text{phase}}^{n+1} &= \mathbf{x}_{3\text{D}} + U^{1/2} [\mathbf{k}_{\text{phase}}^n - \alpha (2 \cdot U^{1/2} A^T (A \mathbf{x}_{\text{phase}}^n \\ &\quad - \mathbf{b}_{\text{phase}}) + \lambda \cdot U^{1/2} \nabla \text{TV}(\mathbf{x}_{\text{phase}}^n))] \\ &= \mathbf{x}_{3\text{D}} + U^{1/2} \mathbf{k}_{\text{phase}}^n - \alpha U [2 \cdot A^T (A \mathbf{x}_{\text{phase}}^n - \mathbf{b}_{\text{phase}}) \\ &\quad + \lambda \cdot \nabla \text{TV}(\mathbf{x}_{\text{phase}}^n)] \\ &= \mathbf{x}_{\text{phase}}^n - \alpha U [2 \cdot A^T (A \mathbf{x}_{\text{phase}}^n - \mathbf{b}_{\text{phase}}) \\ &\quad + \lambda \cdot \nabla \text{TV}(\mathbf{x}_{\text{phase}}^n)], \end{aligned} \quad (\text{A5})$$

which is the gradient decent algorithm for MCIR as shown in Eq. (5).

<sup>a)</sup>Current address: Department of Radiation Oncology, University of Florida, Gainesville, Florida 32610-0385, USA; Electronic mail: parkch@shands.ufl.edu

<sup>b)</sup>Author to whom correspondence should be addressed. Electronic mail: bosong@ucsd.edu; Telephone: +1-858-720-1085; Fax: +1-858-822-5568.

<sup>1</sup>L. Xing, B. Thorndyke, E. Schreibmann, Y. Yang, T. F. Li, G. Y. Kim, G. Luxton, and A. Koong, "Overview of image-guided radiation therapy," *Med. Dosim.* **31**, 91–112 (2006).

<sup>2</sup>L. A. Dawson and D. A. Jaffray, "Advances in image-guided radiation therapy," *J. Clin. Oncol.* **25**, 938–946 (2007).

<sup>3</sup>D. A. Jaffray, "Emergent technologies for 3-dimensional image-guided radiation delivery," *Semin. Radiat. Oncol.* **15**, 208–216 (2005).

<sup>4</sup>D. A. Jaffray, J. H. Siewerdsen, J. W. Wong, and A. A. Martinez, "Flat-panel cone-beam computed tomography for image-guided radiation therapy," *Int. J. Radiat. Oncol., Biol., Phys.* **53**, 1337–1349 (2002).

<sup>5</sup>J. C. Park, S. H. Park, J. H. Kim, S. M. Yoon, S. S. Kim, J. S. Kim, Z. Liu, T. Watkins, and W. Y. Song, "Four-dimensional cone-beam computed tomography and digital tomosynthesis reconstructions using respiratory signals extracted from transcutaneously inserted metal markers for liver SBRT," *Med. Phys.* **38**, 1028–1036 (2011).

<sup>6</sup>W. Song, B. Schaly, G. Bauman, J. Battista, and J. Van Dyk, "Image-guided adaptive radiation therapy (IGART): Radiobiological and dose escalation considerations for localized carcinoma of the prostate," *Med. Phys.* **32**, 2193–2203 (2005).

<sup>7</sup>J. Hatton, B. McCurdy, and P. B. Greer, "Cone beam computerized tomography: The effect of calibration of the Hounsfield unit number to electron density on dose calculation accuracy for adaptive radiation therapy," *Phys. Med. Biol.* **54**, N329–N346 (2009).

<sup>8</sup>S. Yoo and F. F. Yin, "Dosimetric feasibility of cone-beam CT-based treatment planning compared to CT-based treatment planning," *Int. J. Radiat. Oncol., Biol., Phys.* **66**, 1553–1561 (2006).

<sup>9</sup>D. Paquin, D. Levy, and L. Xing, "Multiscale registration of planning CT and daily cone beam CT images for adaptive radiation therapy," *Med. Phys.* **36**, 4–11 (2009).

<sup>10</sup>W. Fu, Y. Yang, N. J. Yue, D. E. Heron, and M. S. Huq, "A cone beam CT-guided online plan modification technique to correct interfractional anatomic changes for prostate cancer IMRT treatment," *Phys. Med. Biol.* **54**, 1691–1703 (2009).

<sup>11</sup>J. P. Bissonnette, T. G. Purdie, J. A. Higgins, W. Li, and A. Bezjak, "Cone-beam computed tomographic image guidance for lung cancer radiation therapy," *Int. J. Radiat. Oncol., Biol., Phys.* **73**, 927–934 (2009).

<sup>12</sup>C. D. Fuller, T. J. Scarbrough, J. J. Sonke, C. R. Rasch, M. Choi, J. Y. Ting, S. J. Wang, N. Papanikolaou, and D. I. Rosenthal, "Method comparison of automated matching software-assisted cone-beam CT and stereoscopic kilovoltage x-ray positional verification image-guided radiation therapy for head and neck cancer: a prospective analysis," *Phys. Med. Biol.* **54**, 7401–7415 (2009).

<sup>13</sup>F. Xu, J. Wang, S. Bai, Y. Li, Y. Shen, R. Zhong, X. Jiang, and Q. Xu, "Detection of intrafractional tumour position error in radiotherapy utilizing cone beam computed tomography," *Radiother. Oncol.* **89**, 311–319 (2008).

<sup>14</sup>M. J. Ghilezan, D. A. Jaffray, J. H. Siewerdsen, M. Van Herk, A. Shetty, M. B. Sharpe, S. Zafar Jafri, F. A. Vicini, R. C. Matter, D. S. Brabbins, and A. A. Martinez, "Prostate gland motion assessed with cine-magnetic resonance imaging (cine-MRI)," *Int. J. Radiat. Oncol., Biol., Phys.* **62**, 406–417 (2005).

<sup>15</sup>E. M. Kerkhof, R. W. van der Put, B. W. Raaymakers, U. A. van der Heide, I. M. Jurgenliemk-Schulz, and J. J. Lagendijk, "Intrafraction motion in patients with cervical cancer: The benefit of soft tissue registration using MRI," *Radiother. Oncol.* **93**, 115–121 (2009).

<sup>16</sup>P. J. Keall, G. S. Mageras, J. M. Balter, R. S. Emery, K. M. Forster, S. B. Jiang, J. M. Kapatoes, D. A. Low, M. J. Murphy, B. R. Murray, C. R. Ramsey, M. B. Van Herk, S. S. Vedam, J. W. Wong, and E. Yorke, "The management of respiratory motion in radiation oncology report of AAPM Task Group 76," *Med. Phys.* **33**, 3874–3900 (2006).

<sup>17</sup>J. J. Sonke, L. Zipp, P. Remeijer, and M. van Herk, "Respiratory correlated cone beam CT," *Med. Phys.* **32**, 1176–1186 (2005).

<sup>18</sup>S. Kriminski, M. Mitschke, S. Sorensen, N. M. Wink, P. E. Chow, S. Tenn, and T. D. Solberg, "Respiratory correlated cone-beam computed tomography on an isocentric C-arm," *Phys. Med. Biol.* **50**, 5263–5280 (2005).

<sup>19</sup>T. Li, L. Xing, P. Munro, C. McGuinness, M. Chao, Y. Yang, B. Loo, and A. Koong, "Four-dimensional cone-beam computed tomography using an on-board imager," *Med. Phys.* **33**, 3825–3833 (2006).

<sup>20</sup>L. Dietrich, S. Jetter, T. Tucking, S. Nill, and U. Oelfke, "Linac-integrated 4D cone beam CT: first experimental results," *Phys. Med. Biol.* **51**, 2939–2952 (2006).

<sup>21</sup>J. Lu, T. M. Guerrero, P. Munro, A. Jeung, P. C. Chi, P. Balter, X. R. Zhu, R. Mohan, and T. Pan, "Four-dimensional cone beam CT with adaptive gantry rotation and adaptive data sampling," *Med. Phys.* **34**, 3520–3529 (2007).

<sup>22</sup>J. J. Sonke, M. Rossi, J. Wolthaus, M. van Herk, E. Damen, and J. Belderbos, "Frameless stereotactic body radiotherapy for lung cancer using four-dimensional cone beam CT guidance," *Int. J. Radiat. Oncol., Biol., Phys.* **74**, 567–574 (2009).

<sup>23</sup>J. J. Sonke, J. Lebesque, and M. van Herk, "Variability of four-dimensional computed tomography patient models," *Int. J. Radiat. Oncol., Biol., Phys.* **70**, 590–598 (2008).

<sup>24</sup>L. A. Feldkamp, L. C. Davis, and J. W. Kress, "Practical cone-beam algorithm," *J. Opt. Soc. Am. A* **1**, 612–619 (1984).

<sup>25</sup>T. Li and L. Xing, "Optimizing 4D cone-beam CT acquisition protocol for external beam radiotherapy," *Int. J. Radiat. Oncol., Biol., Phys.* **67**, 1211–1219 (2007).

<sup>26</sup>F. Bergner, T. Berkus, M. Oelhafen, P. Kunz, T. Pan, and M. Kachelrieß, "Autoadaptive phase-correlated (AAPC) reconstruction for 4D CBCT," *Med. Phys.* **36**, 5695–5706 (2009).

<sup>27</sup>M. Ahmad, P. Balter, and T. Pan, "Four-dimensional volume-of-interest reconstruction for cone-beam computed tomography-guided radiation therapy," *Med. Phys.* **38**, 5646–5656 (2011).

<sup>28</sup>S. Leng, J. Zambelli, R. Tolakanahalli, B. Nett, P. Munro, J. Star-Lack, B. Paliwal, and G. H. Chen, "Streaking artifacts reduction in four-dimensional cone-beam computed tomography," *Med. Phys.* **35**, 4649–4659 (2008).

<sup>29</sup>T. Li, A. Koong, and L. Xing, "Enhanced 4D cone-beam CT with inter-phase motion model," *Med. Phys.* **34**, 3688–3695 (2007).

<sup>30</sup>Q. Zhang, Y. C. Hu, F. Liu, K. Goodman, K. E. Rosenzweig, and G. S. Mageras, "Correction of motion artifacts in cone-beam CT using a patient-specific respiratory motion model," *Med. Phys.* **37**, 2901–2909 (2010).

<sup>31</sup>S. Leng, J. Tang, J. Zambelli, B. Nett, R. Tolakanahalli, and G. H. Chen, "High temporal resolution and streak-free four-dimensional cone-beam computed tomography," *Phys. Med. Biol.* **53**, 5653–5673 (2008).

<sup>32</sup>P. T. Lauzier and G. H. Chen, "Characterization of statistical prior image constrained compressed sensing (PICCS): II. Application to dose reduction," *Med. Phys.* **40**, 021902 (14pp.) (2013).

<sup>33</sup>P. T. Lauzier and G. H. Chen, "Characterization of statistical prior image constrained compressed sensing. I. Applications to time-resolved contrast-enhanced CT," *Med. Phys.* **39**, 5930–5948 (2012).

<sup>34</sup>G. H. Chen, J. Tang, and S. Leng, "Prior image constrained compressed sensing (PICCS): A method to accurately reconstruct dynamic CT images from highly undersampled projection data sets," *Med. Phys.* **35**, 660–663 (2008).

<sup>35</sup>A. H. Andersen and A. C. Kak, "Simultaneous algebraic reconstruction technique (SART): A superior implementation of the art algorithm," *Ultrasound. Imaging* **6**, 81–94 (1984).

<sup>36</sup>J. Bian, J. H. Siewerdsen, X. Han, E. Y. Sidky, J. L. Prince, C. A. Pelizzari, and X. Pan, "Evaluation of sparse-view reconstruction from flat-panel-detector cone-beam CT," *Phys. Med. Biol.* **55**, 6575–6599 (2010).

- <sup>37</sup>K. Choi, J. Wang, L. Zhu, T. S. Suh, S. Boyd, and L. Xing, "Compressed sensing based cone-beam computed tomography reconstruction with a first-order method," *Med. Phys.* **37**, 5113–5125 (2010).
- <sup>38</sup>L. Ritschl, F. Bergner, C. Fleischmann, and M. Kachelrieß, "Improved total variation-based CT image reconstruction applied to clinical data," *Phys. Med. Biol.* **56**, 1545–1561 (2011).
- <sup>39</sup>E. Y. Sidky and X. Pan, "Image reconstruction in circular cone-beam computed tomography by constrained, total-variation minimization," *Phys. Med. Biol.* **53**, 4777–4807 (2008).
- <sup>40</sup>J. C. Park, B. Song, J. S. Kim, S. H. Park, H. K. Kim, Z. Liu, T. S. Suh, and W. Y. Song, "Fast compressed sensing-based CBCT reconstruction using Barzilai-Borwein formulation for application to on-line IGRT," *Med. Phys.* **39**, 1207–1217 (2012).
- <sup>41</sup>J. C. Park, S. H. Park, J. H. Kim, S. M. Yoon, S. Y. Song, Z. Liu, B. Song, K. Kauwelo, M. J. Webster, A. Sandhu, L. K. Mell, S. B. Jiang, A. J. Mundt, and W. Y. Song, "Liver motion during cone beam computed tomography guided stereotactic body radiation therapy," *Med. Phys.* **39**, 6431–6442 (2012).
- <sup>42</sup>W. Y. Song, E. Wong, G. S. Bauman, J. J. Battista, and J. Van Dyk, "Dosimetric evaluation of daily rigid and nonrigid geometric correction strategies during on-line image-guided radiation therapy (IGRT) of prostate cancer," *Med. Phys.* **34**, 352–365 (2007).
- <sup>43</sup>J. C. Park, S. H. Park, J. S. Kim, Y. Han, M. K. Cho, H. K. Kim, Z. Liu, S. B. Jiang, B. Song, and W. Y. Song, "Ultra-fast digital tomosynthesis reconstruction using general-purpose GPU programming for image-guided radiation therapy," *Technol. Cancer Res. Treat.* **10**, 295–306 (2011).
- <sup>44</sup>X. Jia, Y. Lou, J. Lewis, R. Li, X. Gu, C. Men, W. Y. Song, and S. B. Jiang, "GPU-based fast low-dose cone beam CT reconstruction via total variation," *J. X-Ray Sci. Technol.* **19**, 139–154 (2011).
- <sup>45</sup>X. Jia, Y. Lou, R. Li, W. Y. Song, and S. B. Jiang, "GPU-based fast cone beam CT reconstruction from undersampled and noisy projection data via total variation," *Med. Phys.* **37**, 1757–1760 (2010).
- <sup>46</sup>M. A. T. Figueiredo, R. D. Nowak, and S. J. Wright, "Gradient projection for sparse reconstruction: application to compressed sensing and other inverse problems," *IEEE J. Sel. Top. Signal Process.* **1**, 586–597 (2007).
- <sup>47</sup>Z. Qi and G. H. Chen, "Extraction of tumor motion trajectories using PICCS-4DCBCT: A validation study," *Med. Phys.* **38**, 5530–5538 (2011).
- <sup>48</sup>K. Nakagawa, A. Haga, S. Kida, Y. Masutani, H. Yamashita, W. Takahashi, A. Sakumi, N. Saotome, T. Shiraki, K. Ohtomo, Y. Iwai, and K. Yoda, "4D registration and 4D verification of lung tumor position for stereotactic volumetric modulated arc therapy using respiratory-correlated cone-beam CT," *J. Radiat. Res.* **54**, 152–156 (2013).
- <sup>49</sup>M. Chen and R. A. Siochi, "Feasibility of using respiratory correlated mega voltage cone beam computed tomography to measure tumor motion," *J. Appl. Clin. Med. Phys.* **12**, 3473 (2011).
- <sup>50</sup>M. Guckenberger, M. Weininger, J. Wilbert, A. Richter, K. Baier, T. Krieger, B. Polat, and M. Flentje, "Influence of retrospective sorting on image quality in respiratory correlated computed tomography," *Radiother. Oncol.* **85**, 223–231 (2007).
- <sup>51</sup>P. T. Lauzier, J. Tang, and G. H. Chen, "Prior image constrained compressed sensing: implementation and performance evaluation," *Med. Phys.* **39**, 66–80 (2012).
- <sup>52</sup>G. H. Chen, J. Tang, and S. Leng, "Prior image constrained compressed sensing (PICCS)," *Proc. Soc. Photo-Opt. Instrum. Eng.* **6856**, 685618 (2008).
- <sup>53</sup>J. Wang, H. Guan, and T. Solberg, "Inverse determination of the penalty parameter in penalized weighted least-squares algorithm for noise reduction of low-dose CBCT," *Med. Phys.* **38**, 4066–4072 (2011).
- <sup>54</sup>L. Zhu and L. Xing, "Search for IMRT inverse plans with piecewise constant fluence maps using compressed sensing techniques," *Med. Phys.* **36**, 1895–1905 (2009).
- <sup>55</sup>H. Yan, L. Cervino, X. Jia, and S. B. Jiang, "A comprehensive study on the relationship between the image quality and imaging dose in low-dose cone beam CT," *Phys. Med. Biol.* **57**, 2063–2080 (2012).
- <sup>56</sup>F. Bergner, T. Berkus, M. Oelhafen, P. Kunz, T. Pan, R. Grimmer, L. Ritschl, and M. Kachelrieß, "An investigation of 4D cone-beam CT algorithms for slowly rotating scanners," *Med. Phys.* **37**(9), 5044–5053 (2010).
- <sup>57</sup>G. C. Mc Kinnon and R. H. T. Bates, "Towards imaging the beating heart useful with a conventional CT scanner," *IEEE Trans. Biomed. Eng.* **BME-28**(2), 123–127 (1981).
- <sup>58</sup>R. Ning, X. Tang, and D. Conover, "X-ray scatter correction algorithm for cone beam CT imaging," *Med. Phys.* **31**, 1195–1202 (2004).
- <sup>59</sup>M. Sun and J. M. Star-Lack, "Improved scatter correction using adaptive scatter kernel superposition," *Phys. Med. Biol.* **55**, 6695–6720 (2010).
- <sup>60</sup>J. Wang, T. Li, Z. Liang, and L. Xing, "Dose reduction for kilovoltage cone-beam computed tomography in radiation therapy," *Phys. Med. Biol.* **53**, 2897–2909 (2008).